




Commensurate and incommensurate double moiré interference in twisted trilayer grapheneHai Meng ¹, Zhen Zhan ^{1,*} and Shengjun Yuan ^{1,2,†}¹Key Laboratory of Artificial Micro- and Nano-structures of Ministry of Education and School of Physics and Technology, Wuhan University, Wuhan 430072, China²Wuhan Institute of Quantum Technology, Wuhan 430206, China

(Received 21 September 2022; revised 22 December 2022; accepted 23 December 2022; published 6 January 2023)

Twisted graphene multilayers have been recently demonstrated to share several correlation-driven behaviors with twisted bilayer graphene. In general, the van Hove singularities (VHSs) can be used as a proxy of the tendency for correlated behaviors. In this paper, we adopt an atomistic method by combining the tight-binding method with the semiclassical molecular dynamics to investigate the electronic structures of twisted trilayer graphene (TTG) with two independent twist angles. The two independent twist angles can lead to the interference of the moiré patterns forming a variety of commensurate/incommensurate complex supermoiré patterns. In particular, the lattice relaxation, twist angle and angle disorder effects on the VHS are discussed. We find that the lattice relaxation significantly influences the position and magnitude of the VHSs. In the supermoiré TTG, the moiré interference provides constructive or destructive effects depending on the relative twist angle. By modulating the two independent twist angles, novel superstructures, for instance, the Kagome-like lattice, could be constructed via the moiré pattern. Moreover, we demonstrate that a slight change in twist angles (angle disorder) provides a significant suppression of the peak of the VHSs. Apart from the moiré length, the evolution of the VHSs and the LDOS mapping in real space could be used to identify the twist angles in the complicated TTG. In practice, our work could provide a guide for exploring the flat band behaviors in the supermoiré TTG experimentally.

DOI: [10.1103/PhysRevB.107.035109](https://doi.org/10.1103/PhysRevB.107.035109)**I. INTRODUCTION**

When stacking two or more two-dimensional van der Waals materials with a lattice mismatch or a relative twist angle, a moiré superlattice is formed [1]. For some moiré superlattices, a distinguishing feature is the appearance of flat bands at charge neutrality for which the renormalized Fermi velocity is zero, resulting in the Coulomb interaction strength to significantly exceed the kinetic energy of electrons in the flat band, favoring electron-electron correlations [2]. Flat bands appear in twisted bilayer graphene (TBG) with the twist angle equals 1.05° , termed the first magic angle, which exhibits a very interesting range of exotic phenomena including Mott insulating [3], superconductivity [4], ferromagnetism [5], Chern insulators [6], quantum anomalous Hall effect (QAHE) [7], and ferroelectricity [8]. These exciting discoveries have inspired a vast theoretical and experimental search to extend the family of moiré superlattices that exhibit the correlation-driven behaviors, including twisted monolayer-bilayer graphene [9,10], twisted bilayer-bilayer graphene [11,12], trilayer graphene on hexagonal boron nitride [13,14], twisted multilayer graphene [15,16], and transition metal dichalcogenides [17,18]. These moiré superlattices share both similarities and differences with the TBG in symmetries, band topology and interaction strength,

which could help us have a deeper understanding of the correlated behaviors in TBG. Compared to the TBG, some of the moiré superlattices may have practical advantages in fabrication or tunability of the physical properties.

Recently, twisted trilayer graphene (TTG) has gained extensive attention due to the presence of unconventional correlated states [19,20]. In twisted trilayer graphene, new tunable degrees of freedom are introduced by the addition of an extra third layer on the bilayer graphene. For instance, in the TTG with two consecutive twist angles θ_{12} and θ_{23} , the beatings of two bilayer moiré patterns may lead to a more complex supermoiré pattern [21–24]. In fact, the experimental technique to realize the TTG is readily available. Different from the TBG, electronic structures of TTG are highly dependent on the original stacking arrangements and on which layer is twisted [9,25], and are more sensitive to external perturbations [26–28]. In mirror symmetric TTG, a set of dispersive bands coexists with flat bands at charge neutrality, and the magic angle is $\sqrt{2}$ times larger than that of the TBG [29]. Robust and highly tunable superconductivity has been observed in magic angle mirror symmetric TTG [19,20]. It has been reported that TTG without mirror symmetry hosts a variety of correlated metallic and insulating states, and topological magnetic states [9,10,28]. The magic angle of such low symmetry TTG approximates that of the TBG, and possesses correlated states that are asymmetric with respect to the external electric field [10,30].

Compared to the TBG, there are many new challenges in the theoretical calculations of the electronic structures of

*Corresponding author: zhen.zhan@whu.edu.cn

†Corresponding author: s.yuan@whu.edu.cn

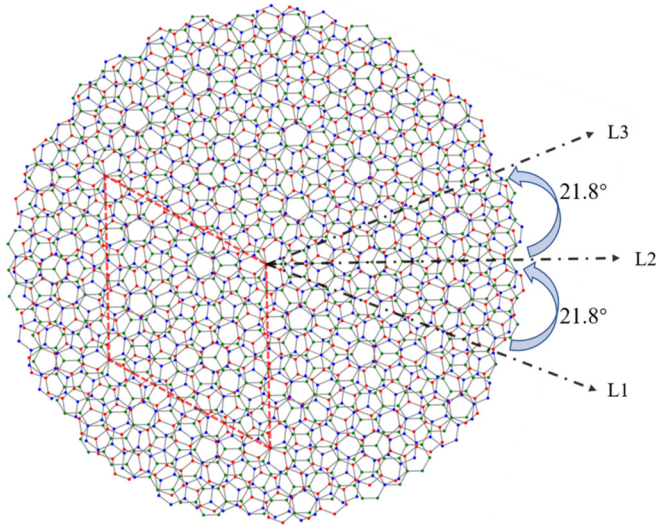


FIG. 1. Schematic of the supermoiré trilayer graphene with $\theta_{12} = \theta_{23} = 21.8^\circ$. The θ_{12} and θ_{23} are twist angles between L1 and L2, L2 and L3, respectively. The atoms in L1 (bottom layer), L2 (middle layer), and L3 (top layer) are represented by red, green, and blue dots, respectively. The unit cell of the moiré supercell is outlined in a red dashed line.

supermoiré TTG: The large size of the moiré pattern and the lack of commensurate supercell for general twist angles. Firstly, the system size becomes much larger. For example, in the mirror symmetric TTG, the number of atoms in a particular twist angle is half more than that of TBG with the same twist angle. When the twist angles are small, the length of the supermoiré period can be extremely large. The case of the mirror-asymmetric TTG with two independent twist angles is even worse. For example, the moiré length of the TTG in Fig. 1 is 2.6 times larger than that of TBG with the same angle. Secondly, because the two twist angles are independent, the supercell description is no longer valid in some cases since the TTG samples become incommensurate.

In theoretical calculations, electronic structures of twisted multilayer graphene are commonly described by effective continuum models [21,29,31,32]. These continuum models with momentum space basis are efficient for computation and require no constraints on the twist angles to construct commensurate supercells. The continuum results show that the van Hove singularities (VHSs) of TTG are significantly dependent on the tuning parameters, for instance, twist angles [21] and original stacking arrangements [31]. Similar to the TBG, the lattice relaxations significantly influence the electronic behaviors of TTG with tiny twist angles and is an important factor to obtain realistic description of the system [33]. Up to now, the lattice relaxation effect is only considered via a continuum model to consider the in-plane distortions and a generalized stacking fault energy to account for the interlayer coupling [29,34]. An atomistic simulation of the lattice relaxation effects on the electronic structures of supermoiré TTG is still missing. In practice, although the control of the global twist angle with a precision of about 0.1 degrees has been achieved, twist-angle variation across different parts of the device with

the order of $\pm 0.01^\circ$ are still exists [35,36]. How will such angle disorder affect the electronic structures of TTG?

In this paper, we systematically investigate the moiré interference in both commensurate and incommensurate TTG. In particular, the lattice relaxation, twist angle and angle disorder effects on the electronic structures of TTG with two independent twist angles are studied. To address the challenges of the lack of periodicity and the large system size, we adopt a round disk method to construct the TTG samples with arbitrary twist angles and calculate the electronic properties via the tight-binding propagation method (TBPM) implemented in our home-made package TBPLaS [37]. The TBPM is based on the numerical solution of time-dependent Schrödinger equation and requires no diagonalization processes. Importantly, both memory and CPU costs scale linearly with the system size. So the TBPM is an efficient method to calculate electronic properties of large-scale and complex quantum systems [33,38,39]. The lattice relaxation is considered via the semiclassical molecular dynamics simulation. We find that the electronic behaviors of TTG are quite sensitive to both the two independent twist angles and angle disorders, in particular for the TTG with mirror symmetry. The systems can have either a constructive or destructive moiré interference depending on the two twist angles. Interestingly, by modulating the angles, novel states, for instance the kagome-like states can be constructed in TTG. The VHSs and local density of states (LDOS) mapping can be utilized as quantities to identify the twist angles of TTG in case that the unit cell size corresponds to a range of different possible sets of twist angle pairs.

This paper is organized as follows. In Sec. II, we introduce the notation and the geometry of the twisted trilayer graphene, the TB model and the computational methods. In Sec. III, for different twist angle configurations, we show the low-energy density of states as a function of twist angle for TTG with and without lattice relaxation. The real space distribution of the electron states of energies at VHS near charge neutral point for different twist angle configurations are also investigated. In Sec. IV, we discuss the effect induced by the twist angle disorder on the VHS. Finally, we give a summary of our work.

II. GEOMETRY AND NUMERICAL METHODS

A. Moiré structure

As shown in Fig. 1, we use a round disk method to construct the TTG with arbitrary twist angles. The two independent twist angles θ_{12} and θ_{23} are chosen to be the rotation of the second layer L2 relative to the first layer L1 and the rotation of the third layer L3 relative to the second layer L2, respectively. The rotation origin is chosen at an atom site. We use a twist angle pair $(\theta_{12}, \theta_{23})$ as the notation for different twist angle configurations. Positive (negative) values of the twist angle denotes counterclockwise (clockwise) rotations. The sample with $(-\theta, \theta)$ has a mirror symmetry with the middle layer as the mirror plane. Figure 1 shows the $(21.8^\circ, 21.8^\circ)$ configuration of twisted trilayer graphene.

For twisted bilayer honeycomb structures, graphene on hexagonal boron nitride (hBN) for instance, an expression for

the period of moiré pattern is given by

$$\lambda = a \frac{1 + \delta}{\sqrt{2(1 + \delta)(1 - \cos \theta) + \delta^2}}, \quad (1)$$

where a is the lattice constant of graphene, δ is the lattice mismatch between the two two-dimensional (2D) materials. The relative rotation ϕ between the moiré pattern and the reference layer is given by

$$\tan \phi = \frac{\sin \theta}{(1 + \delta) - \cos \theta}. \quad (2)$$

For TBG, lattice mismatch $\delta = 0$ and Eqs. (1) and (2) can be simplified as

$$\lambda = \frac{a}{2 \sin(\theta/2)},$$

$$\tan \phi = \frac{\sin \theta}{1 - \cos \theta}. \quad (3)$$

In twisted trilayer graphene, supermoiré patterns arise from the interference between the two bilayer moiré patterns. From Eq. (3), the bilayer moire period λ_{12} (λ_{23}) and their relative rotation θ_m are

$$\lambda_{ij} = \frac{a}{2 \sin |\theta_{ij}/2|},$$

$$\theta_m = |\theta_{12} + \theta_{23}|/2. \quad (4)$$

If $-\theta_{12} \neq \theta_{23}$, there is a mismatch between these two moiré pattern. Then by substituting λ_{12} , λ_{23} , and θ_m into Eq. (1), the trilayer supermoiré period can be obtained. When $\theta_{12} \cdot \theta_{23} > 0$:

$$\lambda_{\text{MoM}} = \frac{a}{2} \left[\frac{3}{2} + \frac{\cos(\theta_{12} + \theta_{23})}{2} - \cos \theta_{12} - \cos \theta_{23} \right]^{-\frac{1}{2}} \quad (5)$$

and when $\theta_{12} \cdot \theta_{23} < 0$ and $-\theta_{12} \neq \theta_{23}$:

$$\lambda_{\text{MoM}} = \frac{a}{2} \left[\frac{1}{2} - \frac{\cos(\theta_{12} + \theta_{23})}{2} \right]^{-\frac{1}{2}} \quad (6)$$

The real space period of the supermoiré pattern of small angle twisted trilayer graphene is very large in most cases. Moreover, for general twist angle pairs, a commensurate supercell does not exist. To calculate the property of these large scale systems with arbitrary twist angles, we construct the system in a large round disk. The radius of the disk should be set sufficiently large to rid the effects of edge states [38] and to cover the large moiré period. In the actual calculation, the disk with radius of 172.2 nm ($700a$) and contains 10 million carbon atoms are large enough for the twist angles investigated in the paper.

B. Lattice relaxation

In the round disk model, carbon atoms at the edge of the disk has dangling bonds which destabilize the system in the process of relaxation. Thus the edge carbon atoms are passivated by hydrogen atoms to saturate the dangling σ edge bonds. The passivation is implemented by placing in-plane hydrogen atoms for each graphene layer near carbon atoms possessing dangling bond. The carbon-hydrogen bond length

is assumed to be 0.1 nm [40]. For the simulation of the structure relaxation, we employ the classical molecular dynamics simulation package LAMMPS [41] to do the full lattice relaxation. Intralayer C-C and C-H interactions are simulated with REBO potential [42]. Interlayer C-C interaction are simulated with the kolmogorov/crespi/z version of Kolmogorov-Crespi potential [43]. This method has been used to study the atomic relaxation effect of other twisted multilayer graphene structures [38,44].

C. Tight-binding model

In this paper, we use a parameterized full tight-binding (TB) scheme for our calculation [45]. The form of the Hamiltonian of twisted trilayer graphene (tTG) can be written as

$$H = \sum_i \epsilon_i |i\rangle \langle i| + \sum_{(i,j)} t_{ij} |i\rangle \langle j|, \quad (7)$$

where $|i\rangle$ is the p_z orbital located at \mathbf{r}_i , and $\langle i, j \rangle$ is the sum over index i and j with $i \neq j$. The hopping integral t_{ij} , interaction between two p_z orbitals located at \mathbf{r}_i and \mathbf{r}_j is [46]

$$t_{ij} = n^2 V_{pp\sigma}(r_{ij}) + (1 - n^2) V_{pp\pi}(r_{ij}), \quad (8)$$

where $r_{ij} = |\mathbf{r}_j - \mathbf{r}_i|$ is the distance between i and j sites, with n as the direction cosine along the direction \mathbf{e}_z perpendicular to the graphene layer. The Slater and Koster parameters $V_{pp\pi}$ and $V_{pp\sigma}$:

$$V_{pp\pi}(r_{ij}) = -\gamma_0 e^{q_\pi(1-r_{ij}/d)} F_c(r_{ij}),$$

$$V_{pp\sigma}(r_{ij}) = \gamma_1 e^{q_\sigma(1-r_{ij}/h)} F_c(r_{ij}), \quad (9)$$

where $d = 1.42 \text{ \AA}$ and $h = 3.349 \text{ \AA}$ are the nearest in-plane and out-of-plane carbon-carbon distances, respectively, γ_0 and γ_1 are commonly reparameterized to fit different experimental results [47,48]. Here we set $\gamma_0 = 3.2 \text{ eV}$ and $\gamma_1 = 0.48 \text{ eV}$. The parameters q_σ and q_π satisfy $\frac{q_\sigma}{h} = \frac{q_\pi}{d} = 2.218 \text{ \AA}^{-1}$, and the smooth function is $F_c(r) = (1 + e^{(r-r_c)/l_c})^{-1}$, where l_c and r_c are chosen as 0.265 and 6.14 \AA , respectively. We only consider the interlayer hoppings between adjacent layers.

D. The density of states and quasidegenstates

Each round disk contains more than ten millions of atoms, which is beyond the capability of commonly used density-functional theory and TB based on diagonalization process. We adopt the TBPM to calculate electronic properties of TTBG in a round disk [49,50]. For the density of states (DOS), the detailed formula is

$$D(\epsilon) = \frac{1}{2\pi S} \sum_{p=1}^S \int_{-\infty}^{\infty} e^{i\epsilon t} \langle \varphi_p(0) | e^{-iHt} | \varphi_p(0) \rangle dt, \quad (10)$$

where $|\varphi_p(0)\rangle$ is one initial state which is the random superposition of all basis states, S is the number of random initial states. The calculation error vanishes with \sqrt{SN} [49]. N is the dimension of the Hamiltonian matrix which equals to the number of atoms in the graphene tight-binding model. In the round disk TTBG with radius of 172 nm, the number of atoms is around 10 million. Thus, in real calculation, a relatively small

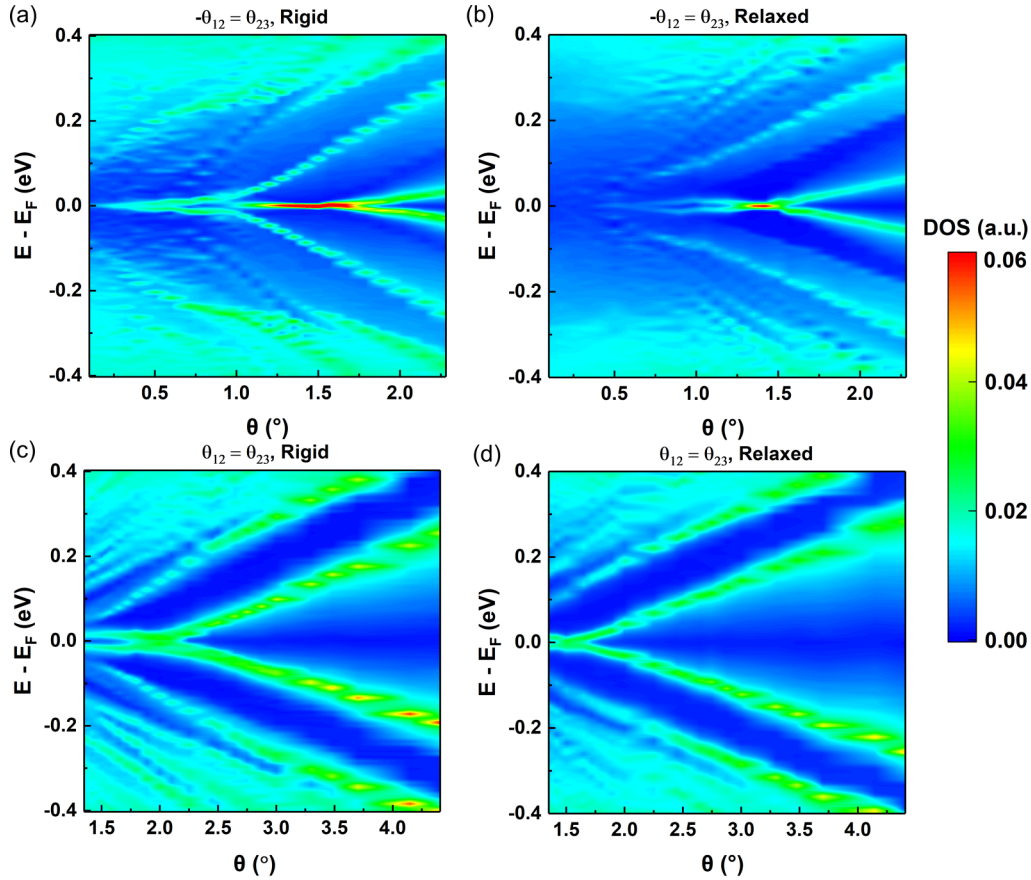


FIG. 2. The density of states (DOS) as a function of twist angles varying from 0.1° to 2.28° for $-\theta_{12} = \theta_{23}$ in (a) rigid and (b) relaxed twisted trilayer graphene. The DOS as a function of twist angles varying from 1.35° to 4.4° for $\theta_{12} = \theta_{23}$ in (c) rigid and (d) relaxed twisted trilayer graphene.

finite value of S is sufficient to obtain a convergent results. We use the same simulation parameters in all the calculations.

The distribution of states in real space can be obtained by calculating the quasieigenstates [50] (a superposition of degenerate eigenstates with certain energy). The quasieigenstates has the expression

$$|\Psi(\varepsilon)\rangle = \frac{1}{\sqrt{\sum_n |A_n|^2 \delta(\varepsilon - E_n)}} \sum_n A_n \delta(\varepsilon - E_n) |n\rangle, \quad (11)$$

where A_n are random complex numbers with $\sum_n |A_n|^2 = 1$, E_n is the eigenvalue, and $|n\rangle$ is the corresponding eigenstate. The local density of states (LDOS) mapping calculated from the quasieigenstates is highly consistent with the experimentally scanning tunneling microscopy dI/dV mapping [33].

III. TUNING THE ELECTRONIC STATES BY TWIST ANGLES

In this part, we investigate the twist angle and lattice relaxation effects on the electronic properties of TTG. As we mentioned before, the structures of TTG are strongly dependent on the original stacking arrangements and on which layer is twisted. Here we mainly focus on two different cases: Case I is the samples with $-\theta_{12} = \theta_{23}$, which have mirror symmetry; case II is a stack of graphene layers where each layer is rotated by a constant amount with respect to the previous one. Each

sample in case II has two consecutive twist angles with $\theta_{12} = \theta_{23}$. In case I, the moiré length of the TTG is equal to that of TBG with the same twist angle, whereas the moiré length of TTG in case II is much larger than both of the bilayer moiré lengths due to the interference between the two bilayer moiré patterns. For example, according to the Eq. (5), if $\theta_{12} = \theta_{23} = 4.4^\circ$, the moiré length of the TTG is around 41.7 nm. For a sample in case I with $-\theta_{12} = \theta_{23} = 4.4^\circ$, the moiré length is only around 3.2 nm. The density of states as a function of twist angle θ are calculated to explore the evolution of the van Hove singularities and the lattice relaxation effects. Due to the incommensurate feature in both cases, we use the round disk model with radius of 172 nm in all calculations. Previous results have been shown that the radius of 172 nm is large enough to get rid of the influence of the edge states [38]. In the round disk method, commensurate or incommensurate systems with any twist angles can be constructed. Therefore an open boundary is adopted in the calculations.

We first discuss the common features emerging in these two different cases. As shown in Fig. 2, the twist angles significantly modulate the energy position of VHS. The red regions represent VHSs. As the twist angle decreases, the VHS gap decreases first to reach a minimum where the magic angle appears, and then increases in some cases. Moreover, the lattice relaxation obviously modifies the DOS of TTG with tiny twist angles. For samples in case I without lattice

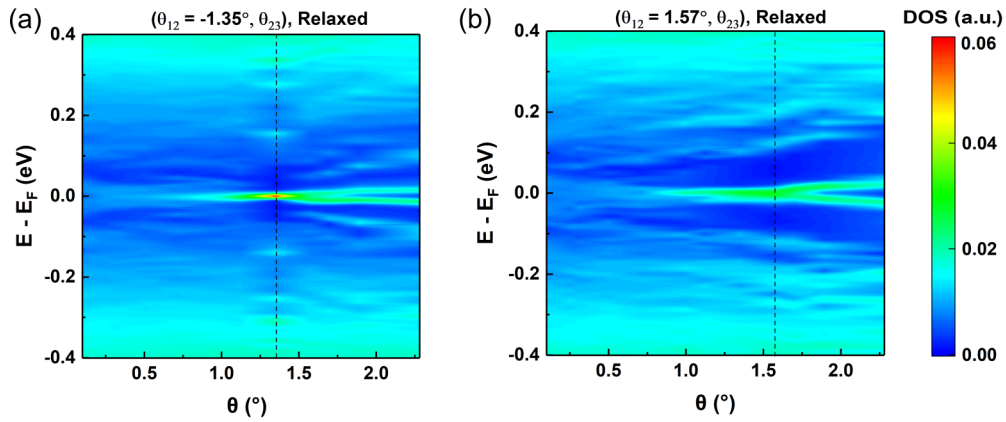


FIG. 3. (a) The DOS as a function of θ_{23} and $\theta_{12} = -1.35^\circ$ in case I of TTG. The vertical dashed line corresponds to the case of $\theta_{23} = 1.35^\circ$. (b) The DOS as a function of θ_{23} and $\theta_{12} = 1.57^\circ$ in case II of TTG. The vertical dashed line corresponds to the case of $\theta_{23} = 1.57^\circ$.

relaxation (rigid), shown in Fig. 2(a), two VHSs near charge neutral point (CNP) have their gap narrowing as twist angle θ decreases, and merge at CNP when angle approaches $\theta = 1.5^\circ$ where the DOS reaches the maximum magnitude. We name this angle the magic angle. In fact, a sharp DOS peak located at the CNP appears when $1.2^\circ \leq \theta \leq 1.6^\circ$. With the angle continually decreasing, the VHS gap first increases and then decreases with VHSs merge again at $\theta = 0.3^\circ$. When consider the lattice relaxation (relaxed) in case I, shown in Fig. 2(b), the evolution of the VHS gap shows similar tendency as the rigid case. The VHSs merge at CNP and reaches maximum (red area) at the magic angle 1.35° . The VHS then splits and diminishes as θ continues to decrease. Compared to the rigid case, the relaxed samples exhibit a narrower range of magic angles, and have VHSs with reduced magnitudes in case of tiny twist angles. In the case of twisted multilayer graphene with alternating relative twist angles $\pm\theta$, the Hamiltonian for the multilayer graphene can be exactly mapped to a set of decoupled bilayers with different angles [51]. The magic angles of these multilayer systems are also related to the TBG. For example, the magic angle of the TTG with $-\theta_{12} = \theta_{23} = 1.5^\circ$ is $\sqrt{2}$ times larger than the bilayer magic angles [25,29].

Compared with $(-\theta, \theta)$ structures, VHSs evolve differently in (θ, θ) structures as shown in Figs. 2(c) and 2(d). For samples in case II, adjacent layers form two identical bilayer moiré periods with a relative rotation of θ forming a supermoiré. The length of the supermoiré period inversely proportional to $1/\theta^2$. Via the rigid sample, we could directly study the supermoiré features in the electronic structures. As shown in Fig. 2(c), the DOS peaks in case II are lower than that of case I. As θ decreases, the VHS gap narrows and reaches minimum (20 meV) at 2.1° but the two VHSs never merge at CNP. This result shows agreement with previous study with a continuum model approach [21]. In the case of systems with $\theta_{12} = \theta_{23}$, if the origin of the VHSs is the TBG plus a perturbation potential from a third layer, in principle, the VHSs merge at 1.72° [21]. Such discrepancy suggests that the VHS behaviors are similar to the case of TBG, which changes the VHSs by tuning the hybridization strength between the two identical TBG. Furthermore, no obviously higher order supermoiré feature is observed in case II,

which is different from the graphene encapsulated by hexagonal boron nitride (hBN). In hBN/graphene/hBN supermoiré, additional Dirac-like points that induced by higher order supermoiré periods are observed [23,24]. These features in case II could be verified by the LDOS mapping in Fig. 4. When the lattice relaxation is considered, shown in Fig. 2(d), the VHSs merge at CNP at 1.57° . The lattice relaxation enforce the system toward a lower energy stacking, for example, the mirror symmetry stacking structure. The states of the VHS in the CNP is mainly localized in the AAA stacking region, as shown in Fig. 4.

Next, we investigate the case of $|\theta_{12}|$ away from $|\theta_{23}|$. For general twist angles, Fig. 3 shows the DOS of relaxed samples as a function of θ_{23} and fixed θ_{12} . In case I with $\theta_{12} = -1.35^\circ$, when $\theta_{23} = 1.8^\circ$, the VHS gap has a value of 30 meV. With θ_{23} decreasing to the magic angle 1.35° , the first and second VHSs approach the CNP and the first VHS merge at the CNP when $\theta_{23} = 1.35^\circ$. When the θ_{23} continually decreases, a sharp DOS peak still appears at the CNP but with a lower magnitude due to the destructive interference effects from the superlattice between 2–3 layer pair. For the sample with $\theta_{23} = -\theta_{12}$ where the top and bottom layers are perfectly aligned, there is a strong increases in the DOS due to the constructive interference effects. For the $|\theta_{23}|$ not equal to $|\theta_{12}|$, the TTG can be mapped to a TBG plus a perturbation potential induced from a third layer. For the sample with θ_{23} around 2° , the two VHSs near the CNP come from the TBG with $\theta = 1.35^\circ$. If we use the presence of VHS as a proxy for electronic correlations, such correlation-driven behavior is extremely sensitive to a slight change in twist angles, which is similar to previous results [22]. Figure 3(b) shows DOS of relaxed structures in case II with different θ_{23} and fixed $\theta_{12} = 1.57^\circ$. As θ increases from magic angle 1.57° , VHSs split with the gap becomes wider, and the magnitude of the VHS becomes smaller. As θ decreases from 1.57° , the VHS has a decrease of its magnitude and vanishes as θ approaches 0° . Similar to case I, for θ_{23} equals to the magic angle, the VHS suffers a constructive interference effect from these two bilayer moiré patterns. For θ_{23} away from the magic angle, the electronic structures can be understood as a magic angle TBG with a destructive interference from the second bilayer moiré structure. However, the TTG in case II is less sensitive

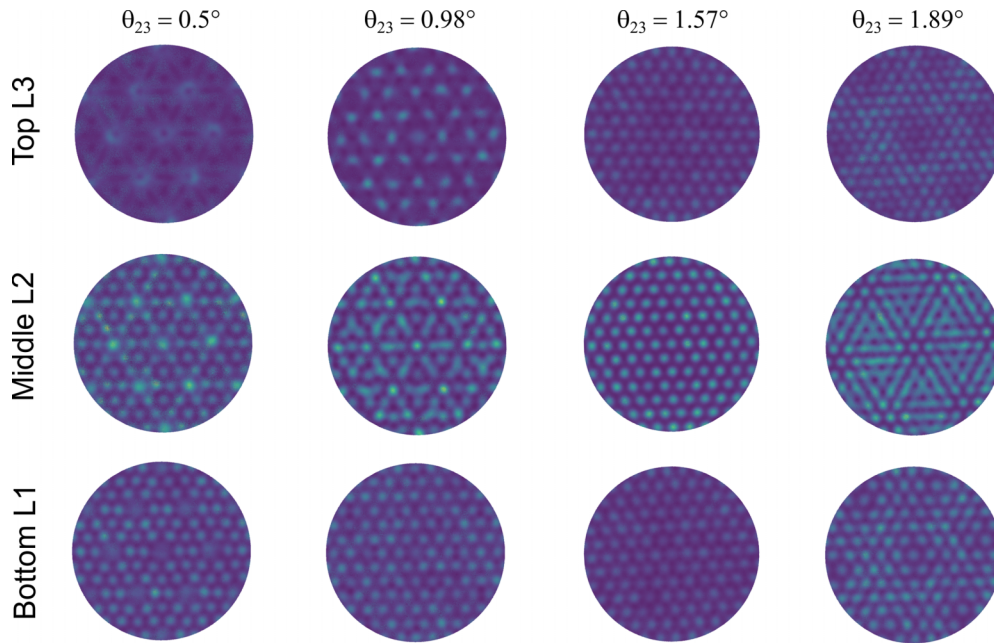


FIG. 4. The calculated LDOS mapping of relaxed structures in case II with different θ_{23} and fixed $\theta_{12} = 1.57^\circ$. Energies are selected at VHS in the vicinity of CNP. Brighter area indicates larger density.

to the angle disorder than case I. For TBG and TTG with mirror symmetry, the twist angle can be identified from the moiré length since the unit cell size corresponds to a unique set of twist angles. On the contrary, for TTG without mirror symmetry, a given unit cell size corresponds to a range of different possible sets of twist angle pairs. In this case, the twist angle can be identified by the above VHS evolution with twist angles in experiment.

The LDOS mapping is another quantity that can be used to identify the twist angles in experiment. The calculated LDOS mapping of relaxed structures in case II with $(1.57^\circ, \theta)$, as shown in Fig. 4, demonstrate the effect of the periodic potential of the moiré pattern on the localization of states in real space. We focus on the energies at the van Hove peaks near the charge neutral point in the DOS and show the mapping of the three graphene layers separately. In TTG, the length of the bilayer moiré period formed by adjacent graphene layers is $a/2 \sin(\theta_{ij}/2)$. Smaller relative twist angle gives larger moiré period. In the configuration of $(1.57^\circ, \theta)$, the bottom and middle layers with twist angle of 1.57° forms a moiré period of length $\lambda_1 = 8.98$ nm, the middle and top layers with twist angle of θ_{23} forms a moiré period of length $\lambda_2 = a/2 \sin(\theta_{23}/2)$. Since the ratio of the two moiré lengths determines the features of the LDOS mapping, we categorize the mapping results into four types.

For type A illustrated in Fig. 4 with $\theta_{23} = 0.5^\circ$, λ_2 is much larger than λ_1 , the VHS states are mainly localized on the middle and bottom layers. It is obvious that in the limit $\theta_{12} \gg \theta_{23}$, TTG decomposes into a decoupled TBG moiré supercell and a graphene monolayer. The top layer does not contribute significantly to the electronic structures in the low-energy range. That is, the TTG can be considered as a magic angle TBG modified by an effective potential from the third layer. In the middle layers, features of both moiré patterns are shown, and the localization is enhanced where the AA

areas of both moiré patterns coincide. For type B with the ratio of the moiré length λ_2/λ_1 around 1.6, for instance $\theta_{23} = 0.98^\circ$, the bottom and top layers show features of bilayer (2L) moiré pattern slightly affected by the other outer layer, the middle layer gives a new complex supermoiré pattern with period λ_3 larger than both 2L moiré periods. For type C with $\theta_{23} = 1.89^\circ$, the mapping features are similar to that of type B. The middle layers also clearly show supermoiré patterns much larger than both 2L moiré patterns. For type D with $\theta_{23} = \theta_{12}$, the moiré length ratio value λ_1/λ_2 is 1. The states of the VHS are mainly localized in the AAA stacking region. The LDOS mappings only show bilayer magic angle features, and the VHS states are mainly localized in the middle layer. No additional moiré period is observed, which further justify that the electronic structures of TTG in case II can be described by the hybridization between the two bilayer moiré patterns. Obviously, the LDOS mapping is highly dependent on twist angles. By tuning the twist angles, new novel superstructures could be constructed. For instance, in case II with $\theta_{12} = 1.57^\circ$ and $\theta_{23} = 0.98^\circ$, a Kagome-like lattice based on moiré pattern are constructed on the top layer. All in all, for the case $\theta_{12} \approx \theta_{23}$, the systems suffer a strong moiré interference, and the VHS states are mainly localized in the middle layer. For $\theta_{12} \gg \theta_{23}$, the systems have a weak moiré interference, and can be decomposed into a TBG with θ_{12} and a graphene monolayer.

IV. TWIST ANGLE DISORDER

Stacking two 2D materials to an arbitrary angle with a precision of 0.1° is still challenging in experiment. Even using the 'tear and stack' technique to fabricate the moiré superlattices, twist-angle disorders are still unavoidable from the nonuniformity of the twist angle across the large-scale sample in experiments. In fact, in a high-quality graphene

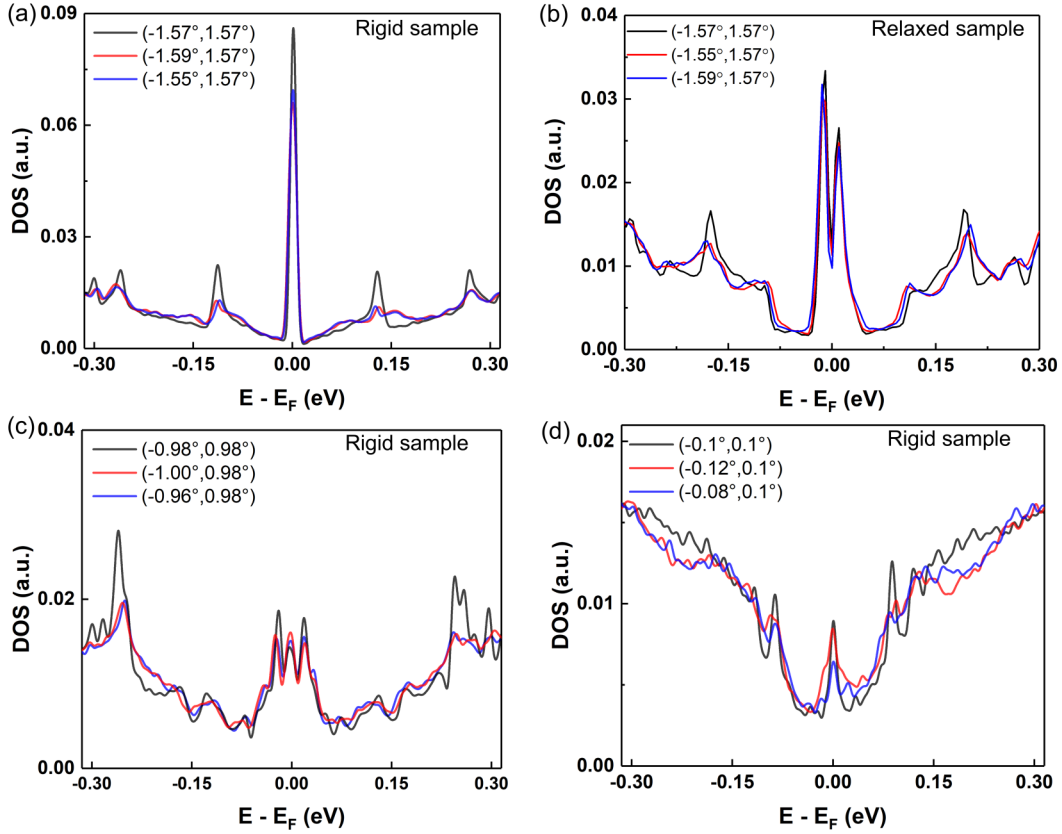


FIG. 5. Comparison of the DOS of TTBG with $(-\theta_{12}, \theta_{23})$ (black line) and with θ_{12} increased (red line) or decreased (blue line) by 0.02° angle disorder. The angle disorder effects in (a) rigid TTBG with $-\theta_{12} = \theta_{23} = 1.57^\circ$, (b) relaxed TTBG with $-\theta_{12} = \theta_{23} = 1.57^\circ$, (c) rigid TTBG with $-\theta_{12} = \theta_{23} = 0.98^\circ$, and (d) rigid TTBG with $-\theta_{12} = \theta_{23} = 0.1^\circ$.

moiré pattern, the main source of disorder is the variations of twist angles across the sample. Previous results have been demonstrated that the correlated phases are extremely sensitive to a slight change in twist angles [22,35]. The angle disorder may explain why two different samples with identical twist angles manifest quite different electronic properties in experiments. Compared with TBG, the more tunable TTBG has more chance suffering the angle disorder since one has to precisely control more than one angle in a sample during the fabrication process. In TTBG, the moiré length is determined by the two independent twist angles. A small variation of one twist angle could result in a huge increase of the moiré length. Then, how will the angle disorder affect the electronic structures of TTBG? As we mentioned before, we can construct TTBG with arbitrary twist angles by utilizing the round disk method. That is, the twist angles can be continuously tuned no matter whether the system is commensurate or incommensurate. By combining the round disk method with the TBPM, it is convenient to investigate the angle disorder effects. In this part, we discuss the electronic structures of TTBG in the presence of angle disorder. In particular, we focus on the angle disorder effects on the VHSs.

In TTBG structures of case I with $(-\theta, \theta)$ where the two moiré patterns align, we introduce misalignment by an extra twist angle deviation $\Delta\theta = 0.02^\circ$ for θ_{12} , i.e., $(-\theta \pm 0.02^\circ, \theta)$. Figure 5 shows the effect of twist angle disorders on the DOS of TTBG with three different angles $\theta = 1.57^\circ, 0.98^\circ, 0.1^\circ$ where $\theta = 1.57^\circ$ is the magic angle. Let

us first focus on the magic angle case. In rigid magic angle TTBG, with a variation of $\Delta\theta$ in only θ_{12} , the positions as well as the width of the VHS are unaffected, whereas the peaks of the VHSs are remarkably suppressed. If we quantify the angle disorder effects by a “BCS superconducting transition temperature,” which is approximately described as $T_c \propto \exp(-\frac{1}{g\rho(E_{vH})})$, our results suggest that the angle disorder strongly suppresses T_c . In the T_c expression, E_{vH} is the energy of the VHS peak, g is the electron-phonon coupling. In the TTBG of case I, there are three different high-symmetry stackings AAA, ABA, and BAB. The VHSs away from the CNP originate from the interlayer intercalation between layers, and the states are localized in the ABA and BAB regions [25]. The angle disorder destroys these high-symmetry stackings. As a consequence, with an angle disorder introduced, the high energy VHSs are smeared out. On the contrary, in relaxed magic angle TTBG, the positions, width and amplitude of the VHSs are unaffected by the angle disorder. The results in Fig. 5(b) show that the TTBG systems with mirror symmetry are protected against twist angle disorders, which is consistent with previous results [29]. That is, the lattice relaxation enforces the system to restore the mirror symmetry stacking structure. In TTBG with twist angles smaller than magic angles, similar to the magic angle case, the VHS is quite sensitive to the twist angle disorder. For TTBG with $\theta = 0.98^\circ$, the angle disorders smear some peaks located around 0.3 eV in the DOS. Similar to the TBG case, multiple flat bands are observed near the second magic angle [52]. In TTBG with $\theta = 0.1^\circ$, both

the width and the amplitude of the first and second VHS are modulated by the angle disorder.

V. CONCLUSION

In summary, we adopt a real-space and atomistic approach for the simulation of the electronic behavior and the relaxation effect of twisted trilayer graphene for general twist angle pairs. We demonstrate how the position and strength of the VHSs evolve with the twist angle in different situations. We mainly focus on two different structures: one has a mirror symmetry with angle pair $(-\theta, \theta)$ and the other has two consecutive angles with (θ, θ) . Due to the moiré interference, the moiré length of the systems in case II are far more larger than that of case I with the same angle θ . Our results show that the atomic relaxations have significant effects on the VHS properties and the emergence of magic angle. The position of the VHSs are highly dependent on the twist angle. We find that for mirror symmetric $(-\theta, \theta)$ structures, the magic angles are 1.57° in rigid case and 1.35° in relaxed case. For (θ, θ) structures, the magic angles are 2.1° and 1.57° in the absence and presence of lattice relaxations, respectively. In TTG with two independent twist angles, when one of the twist angles deviates from the magic angle within a range, the VHS evolution shows a destructive moiré interference effect from the angle changes, and the VHSs follow only with the magic angle. We then show that the LDOS mappings provide an intuitive real-space representation of the double moiré interference and the resulting large complex supermoiré pattern. We find that the mapping features are closely related to the ratio of the two moiré length. For the case that the two angles are identical, the system suffers a strong moiré interference effect and the VHSs states are mainly localized in the middle layer. For one angle far away from the other, the system has a weak interference and can be decoupled into a TBG and a monolayer graphene. By modulating the twist angles, Kagome-like states are constructed due to the interplay between different layers. More importantly, we could use the LDOS and LDOS mapping to identify the twist angles of the TTG in case that the unit cell size corresponds to a range of different possible sets of twist angle pairs.

For mirror symmetric $(-\theta, \theta)$ TTG that detected superconductivity, we find that the twist angle disorder which breaks the mirror symmetry strongly affects the VHS property. This may explain why two different samples with identical twist angles manifest different electronic properties in experiments. We also find that relaxation weakens the disorder effect. In fact, for such small disorders, relaxation can restore the system to the favorable AA stacking for outer layers. Our results could provide a guide for the experiment to explore the flat band behaviors in supermoiré TTG.

ACKNOWLEDGMENTS

We thank G. Yu for providing the code to generate the round disk TBPLaS. This work was supported by the National Natural Science Foundation of China (Grants

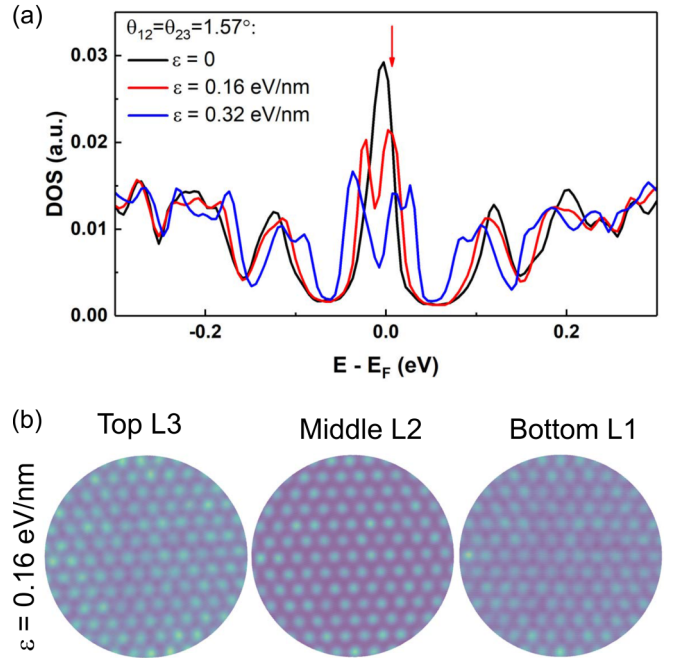


FIG. 6. The external electric field effect. (a) The DOS of the relaxed TTG with $\theta_{12} = \theta_{23} = 1.57^\circ$ under different perpendicular electric fields. (b) The LDOS mapping of the relaxed TTG with $\theta_{12} = \theta_{23} = 1.57^\circ$ under electric field $\varepsilon = 0.16$ eV/nm. The calculated energy is 0.003 eV.

No. 12174291 and No. 12047543). S.Y. acknowledges funding from the National Key R&D Program of China (Grant No. 2018YFA0305800). Numerical calculations presented in this paper have been performed on the supercomputing system in the Supercomputing Center of Wuhan University.

APPENDIX: EXTERNAL ELECTRIC FIELD EFFECT

The electric field can be introduced in the TB calculation by adding an onsite energy term in the Hamiltonian in Eq. (7). The onsite term is defined as

$$H_V = \pm \frac{\varepsilon \hbar}{2} |i\rangle \langle i|, \quad (\text{A1})$$

where $+$ ($-$) corresponds to the top (bottom) layer, ε is the vertical electric field. For example, the electric field effect on the electronic structures of TTG in case I has been studied via the TB model [27,29]. For the TTG with mirror symmetry, a weak vertical electric field reduces the dispersion of the flat bands near the CNP. When the field becomes stronger enough, the flat bands become more dispersive, and start to hybridize with higher-energy bands [27,29]. The TTG in case II has the same tendency. As shown in Fig. 6, the electric field broadens the flat bands. With the strength of the field large enough, the flat bands hybridize the higher-energy bands. Moreover, the flat band states become less localized in the AAA region.

- [1] A. K. Geim and I. V. Grigorieva, *Nature (London)* **499**, 419 (2013).
- [2] R. Bistritzer and A. H. MacDonald, *Proc. Natl. Acad. Sci. USA* **108**, 12233 (2011).
- [3] Y. Cao, V. Fatemi, A. Demir, S. Fang, S. L. Tomarken, J. Y. Luo, J. D. Sanchez-Yamagishi, K. Watanabe, T. Taniguchi, E. Kaxiras *et al.*, *Nature (London)* **556**, 80 (2018).
- [4] Y. Cao, V. Fatemi, S. Fang, K. Watanabe, T. Taniguchi, E. Kaxiras, and P. Jarillo-Herrero, *Nature (London)* **556**, 43 (2018).
- [5] A. L. Sharpe, E. J. Fox, A. W. Barnard, J. Finney, K. Watanabe, T. Taniguchi, M. Kastner, and D. Goldhaber-Gordon, *Science* **365**, 605 (2019).
- [6] K. P. Nuckolls, M. Oh, D. Wong, B. Lian, K. Watanabe, T. Taniguchi, B. A. Bernevig, and A. Yazdani, *Nature (London)* **588**, 610 (2020).
- [7] M. Serlin, C. Tschirhart, H. Polshyn, Y. Zhang, J. Zhu, K. Watanabe, T. Taniguchi, L. Balents, and A. Young, *Science* **367**, 900 (2020).
- [8] D. R. Klein, L.-Q. Xia, D. MacNeill, K. Watanabe, T. Taniguchi, and P. Jarillo-Herrero, [arXiv:2205.04458](https://arxiv.org/abs/2205.04458).
- [9] H. Polshyn, J. Zhu, M. A. Kumar, Y. Zhang, F. Yang, C. L. Tschirhart, M. Serlin, K. Watanabe, T. Taniguchi, A. H. MacDonald *et al.*, *Nature (London)* **588**, 66 (2020).
- [10] S. Xu, M. M. Al Ezzi, N. Balakrishnan, A. Garcia-Ruiz, B. Tsim, C. Mullan, J. Barrier, N. Xin, B. A. Piot, T. Taniguchi *et al.*, *Nat. Phys.* **17**, 619 (2021).
- [11] Y. Cao, D. Rodan-Legrain, O. Rubies-Bigorda, J. M. Park, K. Watanabe, T. Taniguchi, and P. Jarillo-Herrero, *Nature (London)* **583**, 215 (2020).
- [12] M. He, Y. Li, J. Cai, Y. Liu, K. Watanabe, T. Taniguchi, X. Xu, and M. Yankowitz, *Nat. Phys.* **17**, 26 (2021).
- [13] G. Chen, L. Jiang, S. Wu, B. Lyu, H. Li, B. L. Chittari, K. Watanabe, T. Taniguchi, Z. Shi, J. Jung *et al.*, *Nat. Phys.* **15**, 237 (2019).
- [14] G. Chen, A. L. Sharpe, P. Gallagher, I. T. Rosen, E. J. Fox, L. Jiang, B. Lyu, H. Li, K. Watanabe, T. Taniguchi *et al.*, *Nature (London)* **572**, 215 (2019).
- [15] J. M. Park, Y. Cao, L.-Q. Xia, S. Sun, K. Watanabe, T. Taniguchi, and P. Jarillo-Herrero, *Nat. Mater.* **21**, 877 (2022).
- [16] G. W. Burg, E. Khalaf, Y. Wang, K. Watanabe, T. Taniguchi, and E. Tutuc, *Nat. Mater.* **21**, 884 (2022).
- [17] Y. Tang, L. Li, T. Li, Y. Xu, S. Liu, K. Barmak, K. Watanabe, T. Taniguchi, A. H. MacDonald, J. Shan *et al.*, *Nature (London)* **579**, 353 (2020).
- [18] L. Wang, E.-M. Shih, A. Ghiotto, L. Xian, D. A. Rhodes, C. Tan, M. Claassen, D. M. Kennes, Y. Bai, B. Kim *et al.*, *Nat. Mater.* **19**, 861 (2020).
- [19] J. M. Park, Y. Cao, K. Watanabe, T. Taniguchi, and P. Jarillo-Herrero, *Nature (London)* **590**, 249 (2021).
- [20] Y. Cao, J. M. Park, K. Watanabe, T. Taniguchi, and P. Jarillo-Herrero, *Nature (London)* **595**, 526 (2021).
- [21] Z. Zhu, S. Carr, D. Massatt, M. Luskin, and E. Kaxiras, *Phys. Rev. Lett.* **125**, 116404 (2020).
- [22] X. Zhang, K.-T. Tsai, Z. Zhu, W. Ren, Y. Luo, S. Carr, M. Luskin, E. Kaxiras, and K. Wang, *Phys. Rev. Lett.* **127**, 166802 (2021).
- [23] M. Andelković, S. P. Milovanović, L. Covaci, and F. M. Peeters, *Nano Lett.* **20**, 979 (2020).
- [24] Z. Wang, Y. B. Wang, J. Yin, E. Tóvári, Y. Yang, L. Lin, M. Holwill, J. Birkbeck, D. J. Perello, S. Xu, J. Zultak, R. V. Gorbachev, A. V. Kretinin, T. Taniguchi, K. Watanabe, S. V. Morozov, M. Andelković, S. P. Milovanović, L. Covaci, F. M. Peeters, A. Mishchenko, A. K. Geim, K. S. Novoselov, V. I. Fal'ko, A. Knothe, and C. R. Woods, *Sci. Adv.* **5**, eaay8897 (2019).
- [25] Z. Wu, Z. Zhan, and S. Yuan, *Sci. China Phys. Mech. Astron.* **64**, 267811 (2021).
- [26] Z. Wu, X. Kuang, Z. Zhan, and S. Yuan, *Phys. Rev. B* **104**, 205104 (2021).
- [27] A. Lopez-Bezanilla and J. L. Lado, *Phys. Rev. Res.* **2**, 033357 (2020).
- [28] S. Chen, M. He, Y.-H. Zhang, V. Hsieh, Z. Fei, K. Watanabe, T. Taniguchi, D. H. Cobden, X. Xu, C. R. Dean *et al.*, *Nat. Phys.* **17**, 374 (2021).
- [29] S. Carr, C. Li, Z. Zhu, E. Kaxiras, S. Sachdev, and A. Kruchkov, *Nano Lett.* **20**, 3030 (2020).
- [30] Z. Ma, S. Li, Y.-W. Zheng, M.-M. Xiao, H. Jiang, J.-H. Gao, and X. Xie, *Sci. Bull.* **66**, 18 (2021).
- [31] X. Li, F. Wu, and A. H. MacDonald, [arXiv:1907.12338](https://arxiv.org/abs/1907.12338).
- [32] C. Lei, L. Linhart, W. Qin, F. Libisch, and A. H. MacDonald, *Phys. Rev. B* **104**, 035139 (2021).
- [33] H. Shi, Z. Zhan, Z. Qi, K. Huang, E. van Veen, J. Á. Silva-Guillén, R. Zhang, P. Li, K. Xie, H. Ji *et al.*, *Nat. Commun.* **11**, 371 (2020).
- [34] Z. Zhu, P. Cazeaux, M. Luskin, and E. Kaxiras, *Phys. Rev. B* **101**, 224107 (2020).
- [35] A. Uri, S. Grover, Y. Cao, J. A. Crosse, K. Bagani, D. Rodan-Legrain, Y. Myasoedov, K. Watanabe, T. Taniguchi, P. Moon *et al.*, *Nature (London)* **581**, 47 (2020).
- [36] N. P. Kazmierczak, M. Van Winkle, C. Ophus, K. C. Bustillo, S. Carr, H. G. Brown, J. Ciston, T. Taniguchi, K. Watanabe, and D. K. Bediako, *Nat. Mater.* **20**, 956 (2021).
- [37] Y. Li, Z. Zhan, X. Kuang, Y. Li, and S. Yuan, *Comput. Phys. Comm.* **285**, 108632 (2023).
- [38] G. Yu, Z. Wu, Z. Zhan, M. I. Katsnelson, and S. Yuan, *npj Comput. Mater.* **5**, 122 (2019).
- [39] X. Kuang, Z. Zhan, and S. Yuan, *Phys. Rev. B* **103**, 115431 (2021).
- [40] K. S. Subrahmanyam, P. Kumar, U. Maitra, A. Govindaraj, K. P. S. Hembram, U. V. Waghmare, and C. N. R. Rao, *Proc. Natl. Acad. Sci. USA* **108**, 2674 (2011).
- [41] A. P. Thompson, H. M. Aktulga, R. Berger, D. S. Bolintineanu, W. M. Brown, P. S. Crozier, P. J. in 't Veld, A. Kohlmeyer, S. G. Moore, T. D. Nguyen, R. Shan, M. J. Stevens, J. Tranchida, C. Trott, and S. J. Plimpton, *Comput. Phys. Commun.* **271**, 108171 (2022).
- [42] D. W. Brenner, O. A. Shenderova, J. A. Harrison, S. J. Stuart, B. Ni, and S. B. Sinnott, *J. Phys.: Condens. Matter* **14**, 783 (2002).
- [43] A. N. Kolmogorov and V. H. Crespi, *Phys. Rev. B* **71**, 235415 (2005).
- [44] M. M. van Wijk, A. Schuring, M. I. Katsnelson, and A. Fasolino, *2D Mater.* **2**, 034010 (2015).
- [45] G. Trambly de Laissardière, D. Mayou, and L. Magaud, *Phys. Rev. B* **86**, 125413 (2012).
- [46] J. C. Slater and G. F. Koster, *Phys. Rev.* **94**, 1498 (1954).
- [47] F. Guinea and N. R. Walet, *Phys. Rev. B* **99**, 205134 (2019).

- [48] N. Leconte, S. Javvaji, J. An, A. Samudrala, and J. Jung, *Phys. Rev. B* **106**, 115410 (2022).
- [49] A. Hams and H. De Raedt, *Phys. Rev. E* **62**, 4365 (2000).
- [50] S. Yuan, H. De Raedt, and M. I. Katsnelson, *Phys. Rev. B* **82**, 115448 (2010).
- [51] E. Khalaf, A. J. Kruchkov, G. Tarnopolsky, and A. Vishwanath, *Phys. Rev. B* **100**, 085109 (2019).
- [52] X. Lu, B. Lian, G. Chaudhary, B. A. Piot, G. Romagnoli, K. Watanabe, T. Taniguchi, M. Poggio, A. H. MacDonald, B. A. Bernevig *et al.*, *Proc. Natl. Acad. Sci. USA* **118**, e2100006118 (2021).